Monthly Notices
of the
ROYAL ASTRONOMICAL SOCIETY

MNRAS **493,** 4355–4366 (2020)
Advance Access publication 2020 February 27

doi:10.1093/mnras/staa560

Radio morphology–accretion mode link in Fanaroff–Riley type II low-excitation radio galaxies

D. Macconi,[1,2]★ E. Torresi,[2] P. Grandi,[2] B. Boccardi[3] and C. Vignali[1,4]

[1]*Dipartimento di Fisica e Astronomia, Alma Mater Studiorum, Università degli Studi di Bologna, Via Gobetti 93/2, I-40129 Bologna, Italy*
[2]*INAF-Osservatorio di Astrofisica e Scienza dello Spazio di Bologna, Area della Ricerca CNR, Via Gobetti 101, I-40129 Bologna, Italy*
[3]*Max-Planck-Institut für Radioastronomie, Auf dem Hügel 69, D-53121 Bonn, Germany*
[4]*INAF-Osservatorio di Astrofisica e Scienza dello Spazio di Bologna, Via Gobetti 93/3, I-40129 Bologna, Italy*

Accepted 2020 February 19. Received 2020 February 16; in original form 2019 November 26

ABSTRACT

Fanaroff–Riley type II (FR II) low-excitation radio galaxies (LERGs) are characterized by weak nuclear excitation on parsec-scales and properties typical of powerful FR IIs (defined as high-excitation radio galaxies, hereafter HERGs/BLRGs) on kiloparsec-scales. Since a link between the accretion properties and the power of the produced jets is expected both from theory and observations, their nature is still debated. In this work, we investigate the X-ray properties of a complete sample of 19 FR II-LERGs belonging to the 3CR catalogue, exploiting *Chandra* and *XMM–Newton* archival data. We also analyse 32 FR II-HERGs/BLRGs with *Chandra* data as a control sample. We compared FR II-LERG and FR II-HERG/BLRG X-ray properties and optical data available in literature to obtain a wide outlook of their behaviour. The low accretion rate estimates for FR II-LERGs, from both X-ray and optical bands, allow us to firmly reject the hypothesis as they are the highly obscured counterpart of powerful FR II-HERGs/BLRGs. Therefore, at least two hypothesis can be invoked to explain the FR II-LERG nature: (i) they are evolving from classical FR IIs because of the depletion of accreting cold gas in the nuclear region, while the extended radio emission is the heritage of a past efficiently accreting activity; and (ii) they are an intrinsically distinct class of objects with respect to classical FR Is/FR IIs. Surprisingly, in this direction, a correlation between accretion rates and environmental richness is found in our sample. The richer the environment is, the more inefficient is the accretion. In this framework, the FR II-LERGs are intermediate between FR Is and FR II-HERGs/BLRGs both in terms of accretion rate and environment.

Key words: catalogues – galaxies: active – X-rays: galaxies.

1 INTRODUCTION

Black holes (BHs) inhabit the centre of almost all massive galaxies and span a wide range of masses, from 10^6 to several 10^9 $M_\odot$, depending strongly on the properties of the host galaxy (Kormendy 1993; Magorrian et al. 1998; Ferrarese & Merritt 2000; Gebhardt et al. 2000; Tremaine et al. 2002; Kormendy 2004; Greene & Ho 2005, 2006; McConnell et al. 2011)

A small fraction of galaxies (∼1 per cent) show nuclear activity: they are called active galactic nuclei (AGN). AGN produce an enormous amount of energy in a tiny volume (<<pc) via gravitational accretion of matter onto the central BH. About 10 per cent of AGN produce strong relativistic jets, which emit non-thermal radiation over the (almost) whole electromagnetic spectrum; thus, they are defined radio-loud AGN or *jetted* AGN (see Padovani 2016). Radio-loud AGN with strongly boosted emission associated with jets and pointing towards the observer's line of sight are called blazars. Conversely, radio-loud AGN whose jets are oriented close to the plane of the sky are called radio galaxies (RGs).

RGs were classified for the first time by Fanaroff & Riley (1974) following radio morphological criteria. Indeed, Fanaroff–Riley type I objects (FR I) show the highest surface brightness near the core along the jets (i.e. edge-darkened sources), while type II (FR II) objects are characterized by higher surface brightness at the lobes extremities, far from the nucleus (i.e. edge-brightened). There are some cases for which the morphological classification is ambiguous, e.g. they show FR II-like jets, on one side, and FR I-like, on the other: the so-called hybrid double sources (Gopal-Krishna & Wiita 2000).

The FR I–FR II morphological dichotomy quite neatly translates into a separation in terms of extended radio power: Sources with

★ E-mail: duccio.macconi2@unibo.it

radio luminosity at 178 MHz below 10^{26} W Hz^{-1} (Fanaroff & Riley 1974; Tadhunter 2016) are generally FR I, while sources with luminosity above this threshold typically belong to the FR II class.

RGs can be also classified on the basis of their optical spectra, accordingly to the emission lines produced in the narrow-line regions (hereafter NLRs; Laing et al. 1994; Buttiglione et al. 2009, 2010, 2011), in high-excitation or low-excitation radio galaxies (HERGs and LERGs, respectively). The main diagnostic of high excitation is the [O III] λ5007 line luminosity. Conversely, the standard spectroscopic indicators of low excitation are [N II] λ6584, [S II] λ6716, and [O I] λ6364 (Buttiglione et al. 2010). To take into account simultaneously both high- and low-excitation diagnostics, Buttiglione et al. (2010) introduced the excitation index (EI).[1] Considering that different excitation modes of the NLRs are associated to different accretion rates (Gendre et al. 2013; Heckman & Best 2014), this spectroscopic classification reflects the accretion regime at work in the central regions of the AGN. In particular, HERGs accrete efficiently (quasar-mode, $L/L_{\rm Edd} > 0.1$), i.e. the potential energy of the gas accreted by the supermassive black hole (SMBH) is efficiently converted into radiation (Narayan et al. 1998). Conversely, LERGs are characterized by low accretion rates typical of radiatively inefficient hot accretion flows (jet-mode, $L/L_{\rm Edd} \leq 0.01$–0.1), and the jet carries the bulk of the AGN energy output (Narayan et al. 1998; Heckman & Best 2014).

Over the years, studies on radio-loud AGN were fundamental to investigate the jet-launching mechanism and the eventual connection between the ejection of relativistic jets and accretion of material on to the central BH. Indeed, jets are produced close to the BH and their power is predicted to depend on the BH properties (mass and spin) and magnetic field strength: In Blandford & Znajek's (1977a) model, the jet power (P_{jet}) is proportional to $(aMB)^2$, where a is the BH spin, M its mass, and B is the magnetic field value at the BH horizon (Ghisellini et al. 2014).

In any case, the magnetic field plays, in general, a major role in channeling power from the BH (Blandford & Znajek 1977a), or from the disc (Blandford & Payne 1982), into the jet (Maraschi & Tavecchio 2003). In both scenarios, if the magnetic field strength depends, as generally assumed, on the accretion rate (see e.g. Ghisellini et al. 2014), a relation between the accretion rate and the jet power is expected. Various observational studies seem to confirm the link between accretion and ejection (e.g.: Rawlings & Saunders 1991; Celotti, Padovani & Ghisellini 1997; Willott et al. 1999; Maraschi & Tavecchio 2003; Ghisellini 2010; Ghisellini et al. 2014).

In the general picture, FR II radio galaxies host an efficient accretion disc (Shakura & Sunyaev 1973), while FR Is are characterized by hot inefficient accretion flows (ADAF-like; Narayan & Yi 1994; Abramowicz et al. 1995). However, there is a group of FR II sources that do not fit into this framework. They exhibit powerful extended radio structures but inefficient accretion, attested by their optical spectra typical of LERGs. This kind of objects is not so exotic: indeed, about 25 per cent of sources belonging to the 3CR catalogue at $z < 0.3$ and having both radio and optical classifications are FR II-LERGs (Buttiglione et al. 2009, 2010, 2011).

Therefore, given their peculiar nature and not negligible number, FR II-LERGs constitute a particularly relevant population for the comprehension of the role of the central engine in powering RG jets and shaping the extended radio morphology.

Within this context, the X-ray band is a fundamental tool to probe the processes at work on different scales from sub-pc up to several hundreds of kpc. To this aim, we performed a systematic and homogeneous X-ray analysis of all FR IIs belonging to the 3CR sample (Bennett 1962) below z<0.3, one of the best studied radio catalogues in all energy bands. For the first time, FR II-LERGs are explored as a separate class. Their X-ray and multi-frequency properties are compared to those of FR II-HERGs, in order to understand their nature. For example, they could be FR II-HERGs seen through a thicker obscuring screen or they could have central engines in a 'switching-off' phase, in which the standard accretion flow becomes inefficient (ADAF-like). Finally, the role played by the environment in triggering the AGN and the link between environment and jet power are also explored.

This work is organized as follows: In Section 2, we describe the sample of sources. In Section 3, we report on the X-ray data reduction and analysis, and discuss our results in Section 4. In Section 5, we summarize our conclusions. Throughout this paper, we adopt $H_0 = 71$ km s^{-1} Mpc^{-1}, $\Lambda_\Omega = 0.73$, and $\Lambda_{\rm m} = 0.27$ (Komatsu et al. 2009).

2 THE ANALYSED SAMPLE

The 3CR sources at $z < 0.3$ classified both in the optical (HERGs versus LERGs) and radio bands (FR Is versus FR IIs) are 79. Following Buttiglione et al. (2009, 2010, 2011), who provided the classification in both bands, radio galaxies are divided into the following:

(i) 30 FR II-HERGs and 17 FR II-BLRGs[2];
(ii) 19 FR II-LERGs;
(iii) 13 FR Is.

From the radio point of view, the majority of the sources are powerful FR IIs (66), distributed over the entire redshift range, while FR Is (13) represent a small fraction of the total (∼16 per cent) and cluster below $z < 0.05$. This is not surprising since low-power RGs are known to be mainly observed at lower redshifts (Laing, Riley & Longair 1983; Spinrad et al. 1985; Wall & Peacock 1985; Morganti, Killeen & Tadhunter 1993; Burgess & Hunstead 2006a,b). From the optical point of view, the number of HERGs/BLRGs (47) and LERGs (32) is not very different, implying that about half of the local radio sources is characterized by a low-accretion regime, independently of the radio classification. Indeed, FR II-LERGs and FR II-HERGs/BLRGs span similar values of radio luminosity at 178 MHz, as shown in Fig. 1. Following the prescriptions of Willott et al. (1999), if we assume $L_{178\,\rm MHz}$ as a crude signature of the average jet power over time, FR II-LERGs do not fit in the stardand picture, linking powerful jets to efficient accretion flows. Other ingredients have to be considered to explain the observations.

3 X-RAY DATA ANALYSIS

We performed a systematic X-ray analysis of all the FR IIs of the 3CR sample at $z < 0.3$ exploiting archival data from the *Chandra*

[1]The excitation index can be defined as

$$\mathrm{EI} = \log[\mathrm{O\,III}]/\mathrm{H}\beta - 1/3(\log[\mathrm{N\,II}]/\mathrm{H}\alpha + \log[\mathrm{S\,II}]/\mathrm{H}\alpha + \log[\mathrm{O\,I}]/\mathrm{H}\alpha).$$

[2]Broad-lline radio galaxies (BLRGs) are classified as HERGs according to their NLR emission. They differ from HERGs in the presence of broad permitted lines in the optical spectrum, coming from the broad-line regions (BLRs). Therefore, HERGs are classified as type 2 AGN, i.e. edge-on, while BLRGs are type 1s, i.e. face-on.

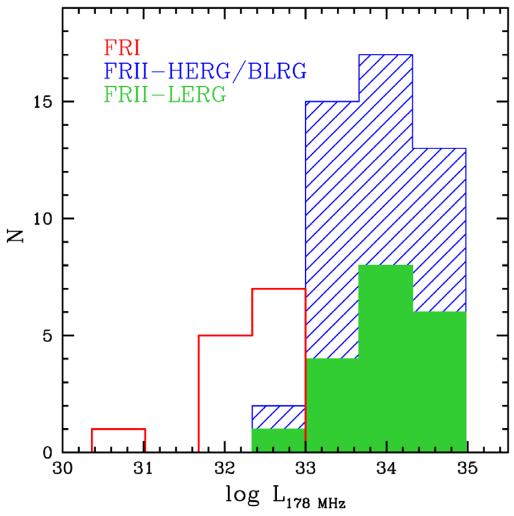

Figure 1. Distribution of total radio luminosity at 178 MHz in units of erg s^{-1} Hz^{-1} from Spinrad et al. (1985): FR II-HERGs/BLRGs are in blue, FR II-LERGs are in green, and FR Is are in red. While a separation between FR Is and FR IIs is clear, FR II-HERGs/BLRGs and FR II-LERGs completely overlap.

satellite. This is the most suited telescope to perform such kind of analysis, given the good angular resolution (≈0.5 arcsec in the observational energy band) and the presence of all the sources of the analysed sample in the public archive.[3] Several of them belong to the 3C *Chandra* legacy survey (Massaro et al. 2010, 2012). However, Massaro et al. adopted a flux sky map method to present the data, while here we follow a different approach based on the direct fit of the data.

We consider FR II-LERGs as key targets of our work (main sample). We also analyse X-ray data of FR II-HERGs/BLRGs as a 'control' sample. The goal of our analysis is to investigate the nuclear activity of sources down to the innermost regions (sub-parsec scales) both in terms of gas presence (N_{HX}) and X-ray luminosity.

In Table 1, the observation log is reported. All the sources were pointed by *Chandra*.

When more than one observation was available, the data were combined in order to achieve better statistics. We also analysed all the FR II-LERGs belonging to the *XMM–Newton* archive. In three cases, i.e. 3C 349, 3C 353, and 3C 460, we used *XMM–Newton* data since its larger effective area guaranteed a better constraint of the spectral parameters.

Chandra data were reprocessed using the software Chandra Iterative Analysis Observations (CIAO) version 4.10, with calibration data base CALDB version 4.8.1, and following standard procedures.

A preliminary check of the images was necessary to investigate the presence of extended emission. In case the source was extended, two images were produced: a soft one (0.3–4 keV) and a hard one (4–7 keV). This approach helps in better defining the pointlike emission from the core and modelling its spectrum. Subsequently, VLA radio contours at 1.4 or 5 GHz (with a few arcseconds as spatial resolution) were superimposed on the hard X-ray image to properly identify the peak of the nuclear emission and verify the presence of other features such as lobes, jets, knots along the jet. Given the coincidence between the radio core and the X-ray peak in all the

[3] https://cda.harvard.edu/chaser/

Table 1. Observation log of FR II-LERGs (main sample) and FR II-HERGs/BLRGs (control sample). Column description: (1) 3CR name; (2) telescope: C = *Chandra* and X = *XMM–Newton*; (3) observation ID; (4) start date of the observation; (5) instrument used in the observation; and (6) total exposure time in seconds. All the sources are the target of the observation.

3CR (1)	Teles. (2)	obsID (3)	Date (4)	CCD (5)	t_{exp} (s) (6)
FR II-LERGs – main sample					
3C 88	C	9391	2008-06-30	ACIS-I	11 270
	C	11751	2009-10-14	ACIS-S	20 180
	C	11977	2009-10-06	ACIS-S	50 280
	C	12007	2009-10-15	ACIS-S	35 080
3C 132	C	9329	2008-03-26	ACIS-S	7790
3C 153	C	9302	2007-12-07	ACIS-S	8170
3C 165	C	9303	2008-02-02	ACIS-S	7770
3C 166	C	12727	2010-11-29	ACIS-S	8050
3C 173.1	C	3053	2002-11-06	ACIS-S	24 310
3C 196.1	C	12729	2011-02-11	ACIS-S	8050
3C 213.1	C	9307	2008-04-14	ACIS-S	8170
3C 236	C	10249	2009-01-14	ACIS-I	41 040
3C 288	C	9275	2008-04-13	ACIS-S	40 150
3C 310	C	11845	2010-04-09	ACIS-S	58 320
3C 326	C	10908	2009-05-10	ACIS-I	27 880
3C 349	X	0501620301	2007-08-07	EPIC/pn	14 863
	X	0501621601	2007-10-03	EPIC/pn	15 113
3C 353	X	0400930101	2006-08-25	EPIC/pn	44 264
	X	0400930201	2007-02-17	EPIC/pn	10 916
3C 357	C	12738	2010-10-31	ACIS-S	8050
3C 388	C	5295	2004-01-29	ACIS-I	31 120
3C 401	C	4370	2002-09-21	ACIS-S	25 170
	C	3083	2002-09-20	ACIS-S	22 960
3C 430	C	12744	2011-11-14	ACIS-S	8050
3C 460	X	0675400101	2011-12-24	EPIC/pn	48 744
FR II-HERGs/BLRGs – control sample					
3C 20	C	9294	2007-12-31	ACIS-S	8040
3C 33	C	7200	2005-11-12	ACIS-S	20 180
3C 61.1	C	9297	2008-12-05	ACIS-S	8160
3C 79	C	12723	2010-11-01	ACIS-S	7790
3C 98	C	10234	2008-12-24	ACIS-I	32 130
3C 105	C	9299	2007-12-17	ACIS-S	8180
3C 133	C	9300	2008-04-07	ACIS-S	8140
3C 135	C	9301	2008-01-10	ACIS-S	8040
3C 136.1	C	9326	2008-01-10	ACIS-S	10040
3C 171	C	10303	2009-01-08	ACIS-S	60 220
	C	9304	2007-12-22	ACIS-S	8040
3C 180	C	12728	2010-12-24	ACIS-S	8060
3C 184.1	C	9305	2008-03-27	ACIS-S	8130
3C 192	C	9270	2007-12-18	ACIS-S	10 150
	C	19496	2017-12-18	ACIS-S	70 110
	C	20888	2017-12-21	ACIS-S	10 070
	C	20889	2017-12-21	ACIS-S	33 110
	C	20890	2017-12-24	ACIS-S	21 410
	C	20891	2017-12-22	ACIS-S	35 760
3C 223	C	12731	2012-01-07	ACIS-S	8050
3C 223.1	C	9308	2008-01-16	ACIS-S	8030
3C 234	C	12732	2011-01-19	ACIS-S	8050
3C 277.3	C	11391	2010-03-03	ACIS-S	25 120
	C	15023	2014-03-15	ACIS-I	44 080
	C	15024	2014-03-16	ACIS-I	20 090
	C	16600	2014-03-11	ACIS-I	98 080
	C	16599	2014-03-13	ACIS-I	29 090
3C 284	C	12735	2010-11-17	ACIS-S	8050
3C 285	C	6911	2006-03-18	ACIS-S	40 150
3C 300	C	9311	2008-03-21	ACIS-S	8040
3C 303.1	C	9312	2008-02-21	ACIS-S	7770

Table 1 – *continued*

3CR (1)	Teles. (2)	obsID (3)	Date (4)	CCD (5)	t_{exp} (s) (6)
3C 305	C	9330	2008-04-07	ACIS-S	8330
	C	12797	2011-01-03	ACIS-S	29 040
	C	13211	2011-01-06	ACIS-S	29 040
3C 321	C	3138	2002-04-30	ACIS-S	47 730
3C 327	C	6841	2006-04-26	ACIS-S	40 180
3C 379.1	C	12739	2011-04-04	ACIS-S	8050
3C 381	C	9317	2008-02-21	ACIS-S	8170
3C 403	C	2968	2002-12-07	ACIS-S	50 130
3C 436	C	9318	2008-01-08	ACIS-S	8140
	C	12745	2011-05-27	ACIS-S	8060
3C 452	C	2195	2001-08-21	ACIS-S	80 950
3C 456	C	12746	2011-01-17	ACIS-S	8050
3C 458	C	12747	2010-10-10	ACIS-S	8050
3C 459	C	12734	2011-10-13	ACIS-S	8050
	C	16044	2014-10-12	ACIS-S	59 960

analysed images, no astrometrical correction was applied. The core spectrum was usually extracted from circular regions with a radius ranging between 1.5 and 2.5 arcsec (depending on the presence or not of extended emission) in order to collect more than 90 per cent of photons. The background was extracted in a clean circular region in the same CCD of the source, avoiding any contamination from field sources or from the source itself.

Spectra were grouped to a minimum of 20 counts per bin in order to adopt the χ^2 statistics. When this was not possible, the C-statistics was applied (Cash 1979) and spectra were grouped to at least one count per bin. For the sources 3C 136.1, 3C 153, and 3C 430, the small number of counts (about 10 counts over the entire spectrum) prevented any modelling. Fluxes and luminosities were estimated using the *Chandra* Proposal Planning Toolkit (PIMMS)[4] and assuming a simple power-law model with $\Gamma = 1.7$ (Grandi, Malaguti & Fiocchi 2006). In 3C 196.1, 3C 288, 3C 310, and 3C 388, the AGN emission is completely overwhelmed by the cluster, thus precluding any nuclear study.

XMM–Newton data were reduced using the Scientific Analysis Software (SAS) version 16.1 together with the latest calibration files and following standard procedures. Throughout the paper, results refer to EPIC/pn data, but all the EPIC instruments were checked.

Source and background spectra were extracted in 0.5–10 keV band from circular regions with radius varying between 20 and 30 arcsec, depending on the source extension, in order to maximize the S/N ratio. In all cases, at least 80 per cent of photons fell within the extraction region. The background was chosen in a circular region in the same CCD of the source, avoiding any contamination from field sources or from the source itself.

Spectra were grouped to a minimum of 20 counts per bin and the χ^2 statistics was applied.

We checked for the presence of pile-up effects in each source (using the PIMMS software for *Chandra* data and the task EPATPLOT in the SAS for *XMM–Newton* data). The pile-up was generally negligible (< 10 per cent) or absent in FR II-LERGs, but turned out to be important in FR II-HERGs/BLRGs seen face-on (i.e. BLRGs). Indeed, we could perform a *Chandra* spectral analysis only for two BLRGs, i.e. 3C 184.1 and 3C 459, for which the estimated pile-up was < 10 per cent.

[4]http://cxc.harvard.edu/toolkit/pimms.jsp

The spectral analysis was performed using the XSPEC version 12.9.1 (Arnaud 1996). The energy range considered in the spectral fitting was 0.3–7 keV for *Chandra* and 0.5–10 keV for *XMM–Newton*. Errors reported are quoted at 90 per cent confidence for one parameter of interest (Avni 1976).

3.1 Spectral analysis

An inspection of the X-ray images indicates that 6 out of 19 FR II-LERGs show strong emission over the galaxy scale (from several tens to hundreds of kpc) due to the hot gas from the cluster (Fig. 2). In contrast, no FR II-HERGs/BLRGs show cluster emission in the *Chandra* images, although some of them show resolved emission on kiloparsec-scale.

At first, we considered as baseline model a single power law convolved with Galactic column density (PHABS; Kalberla et al. 2005). When the power-law spectral slope was less than 1, an intrinsic absorption component (ZPHABS) was added to the fit. Because of the poor statistics and/or the complexity of the emission, we were forced to fix the hard photon index ($\Gamma = 1.7$) in 7 out of 19 FR II-LERGs and 27 out of 32 FR II-HERGs/BLRGs (see Table 2). If no *XMM–Newton/Chandra* information on the power-law spectral slope was available in literature, we chose a reliable value of $\Gamma = 1.7$. Nonetheless, we checked whether different values of the photon indices could produce significant changes in the estimate of the column density. However, even assuming different photon indices ($\Gamma = 1.4$ and 2.0), the column densities and the intrinsic luminosity remain consistent within the errors.[5] If residuals were still present at soft energies, a second power-law, or a thermal emission (MEKAL), was added to the fit. A second power law is expected if the primary component is scattered by clouds of electrons above the torus. A thermal emission is expected if the source is embedded in a gaseous environment, i.e. hot corona of early-type galaxies (Fabbiano, Kim & Trinchieri 1992) or intergalactic medium. The MEKAL model could also roughly mimic features related to photoionized gas, given the limited energy resolution of CCD detectors. Therefore, after testing for collisional gas presence, if prominent photoionized features were still present in the soft X-ray spectrum, a fit with multiple narrow emission lines (Gaussian profile) was tested.

In the hard spectrum, a Gaussian component (ZGAUSS) was included if positive residuals were observed in the region of the iron Kα line (5–7 keV). Once the Fe Kα line was attested, the presence of a reflection component (PEXRAV) was verified: in fact, this is expected when cold matter surrounding the nuclear engine reprocesses the primary X-ray radiation (Lightman & White 1988). In this case, the cut-off energy and the angle between the normal to the disc and the observer were fixed to 100 keV and 30°, respectively. The reflection component is modelled by the parameter $R = \Omega/2\pi$, corresponding to the solid angle fraction of a neutral, plane-parallel slab illuminated by the continuum power law (PEXRAV). Given the low statistics and the limited energy range covered by *Chandra* and *XMM–Newton*, small variations in these parameters do not impact the fit.

[5]For all the sources with fixed spectral slope, the N_H and L_X values do not change, respectively, more than ≈15 and 40 per cent varying the power-law spectral slope from 1.4 to 2.0. As the uncertainties of the same quantities in Table 2 are above 70 per cent, we are confident that the $\Gamma = 1.7$ assumption does not significantly affect our results.

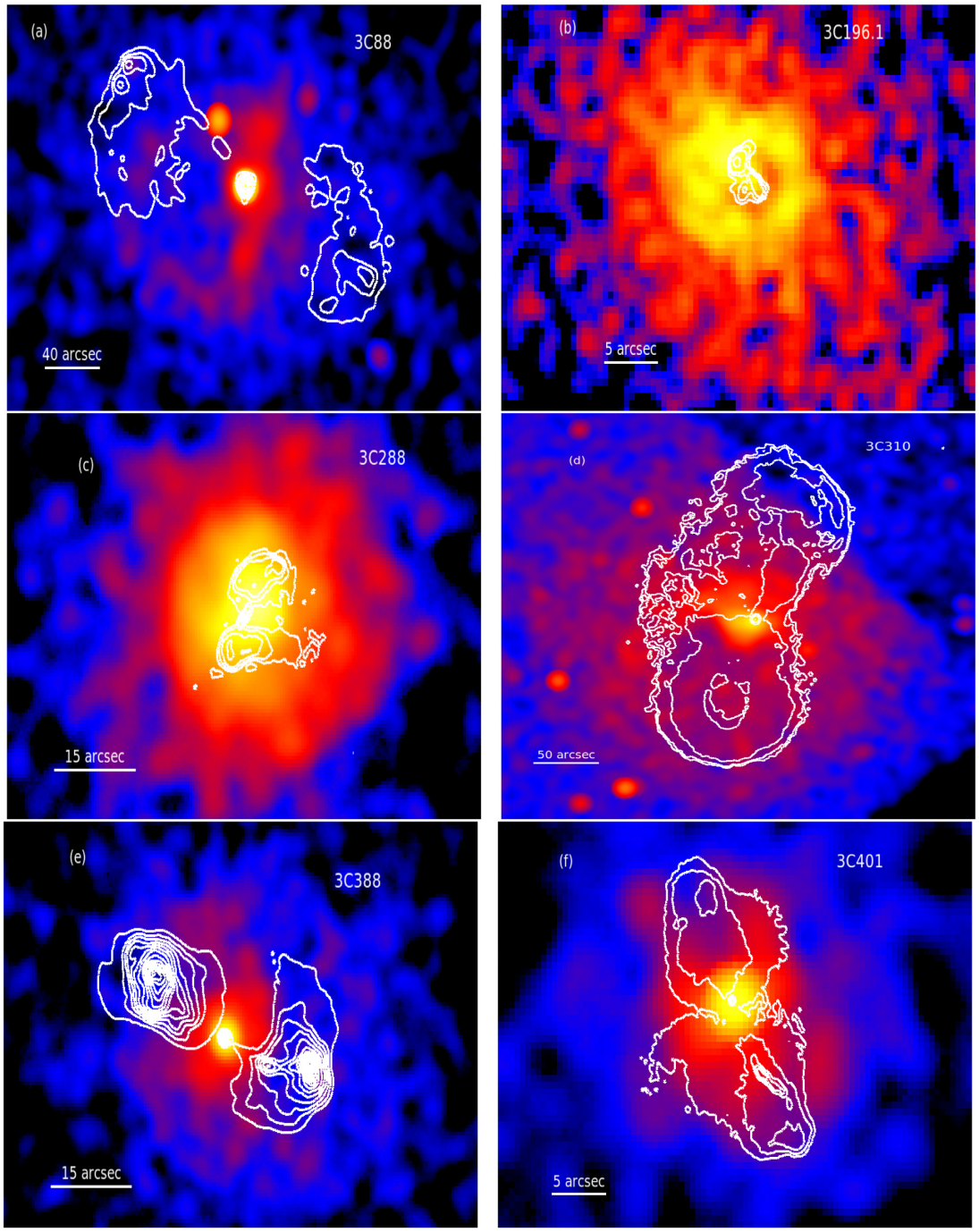

Figure 2. *Chandra* 0.3–7 keV images of extended FR II-LERGs. Radio VLA contours at 5 and 1.4 GHz (white) are superimposed to the X-ray images. Panel (a): 3C 88 inhabits the centre of a galaxy group and produce the largest X-ray cavities ever found in such an environment (Liu et al. 2019). Panel (b): 3C 196.1 is the brightest cluster galaxy of a cool core cluster. Ricci et al. (2018) measured a core cluster temperature $kT\sim$ 3 keV, in agreement with our analysis (see Table 3). Panel (c): 3C 288 resides in the centre of a poor not-CC cluster, as shown by Lal et al. (2010). They found an ICM gas temperature $kT\sim$3 keV extending up to 400 kpc. Panel (d): 3C 310 is the central galaxy of a poor cluster with a temperature of about 3 keV at a distance between 100 and 180 kpc (at which a shock occurs) (Kraft et al. 2012). Panel (e): 3C 388 resides in the centre of a small cluster environment with an ICM temperature of about 3.5 keV and a cool core probably heated by a nuclear outburst (Kraft et al. 2006). Panel (f): 3C 401 is in the centre of a cluster with ICM mean temperature of 2.9 keV. Reynolds, Brenneman & Stocke (2005) proposed both a thermal hot core ($T \approx 4.9$ keV) and a simple power-law model (which is the model assumed in this work) because they are statistically indistinguishable.

3.2 Results

The results of the X-ray analysis, listed in Table 2, are in substantial agreement with those reported in the literature using different satellites and/or different approaches (e.g. Evans et al. 2006; Grandi et al. 2006; Massaro et al. 2010, 2012). Details on the soft X-ray component and reprocessed features are listed in Tables 3 and 4, respectively.

The photon index of FR II-LERGs was tightly constrained for 8 out of 19 sources: the mean Γ value is 1.7 and the standard

Table 2. Spectral parameters of the X-ray continuum.

Name	z	$N_{\rm H,Gal}$ (10^{20} cm^{-2})	Fitted model[a]	$N_{\rm H,intr}$ (10^{22} cm^{-2})	$\Gamma_{\rm H}$	$L_{2-10\,\rm keV}$ (10^{42} erg s^{-1})	Statistics[b]
FR II-LERGs							
3C 88	0.0302	8.3	[iii]	2.0 ± 0.5	1.6 ± 0.3	0.4 ± 0.2	36.9/50
3C 132	0.214	21.3	[ii]	5^{+4}_{-3}	1.7[c]	22^{+12}_{-8}	4.1/5 C
3C 153[d]	0.2769	16.2	[i]	–	1.7[c]	<1.5	–
3C 165	0.2957	19.4	[ii]	3 ± 2	1.7[c]	23^{+11}_{-8}	8.2/14 C
3C 166	0.2449	17.1	[i]	<0.16	1.6 ± 0.2	80 ± 10	20.1/19
3C 173.1	0.292	4.5	[vi]	30^{+200}_{-20}	1.7[c]	27^{+180}_{-16}	35.3/25 C
3C 196.1	0.198	6.0	[vii]	–	–	<9.6	20.5/13 C
3C 213.1	0.1939	2.4	[i]	<0.43	$1.9^{+0.5}_{-0.4}$	4 ± 1	15.4/9 C
3C 236	0.1005	1.0	[ii]	$1.9^{+0.6}_{-0.5}$	1.4 ± 0.3	12^{+7}_{-4}	27.0/29
3C 288	0.246	0.8	[vii]	–	–	<4.7	6.4/6
3C 310	0.0535	3.7	[vii]	–	–	<0.02	10.5/17 C
3C 326	0.0895	9.0	[ii]	$2.2^{+2.8}_{-1.7}$	1.7[c]	$0.2^{+0.2}_{-0.1}$	3.4/3 C
3C 349	0.205	1.9	[ii]	0.9 ± 0.2	1.4 ± 0.2	60 ± 10	46.2/47
3C 353	0.0304	9.3	[vi]	$6.7^{+0.9}_{-0.8}$	1.7 ± 0.2	3 ± 1	58.0/61
3C 357	0.1662	3.1	[iii]	3 ± 2	2 ± 1	22^{+6}_{-12}	17/18 C
3C 388	0.0917	5.5	[vii]	–	–	<0.9	62.5/59 C
3C 401	0.2011	5.9	[i]	<0.16	1.7 ± 0.1	5.0 ± 0.5	15.9/18
3C 430[d]	$0.^{0541}$	33.1	[i]	–	1.7[c]	<0.05	–
3C 460	0.268	4.72	[iii]	25^{+23}_{-11}	1.7[c]	20 ± 10	5.7/6
FR II-HERGs/BLRGs							
3C 20	0.174	18.0	[ii]	15^{+4}_{-3}	1.7[c]	110^{+30}_{-20}	24.1/25 C
3C 33	0.0596	3.4	[v]	53^{+8}_{-7}	1.7[c]	100^{+30}_{-20}	32.5/40
3C 61.1	0.184	7.9	[iii]	29^{+23}_{-12}	1.7[c]	40^{+40}_{-20}	30/18 C
3C 79	0.2559	8.7	[iii]	33^{+12}_{-10}	1.7[c]	270^{+130}_{-90}	14.4/16 C
3C 98	0.0304	10.0	[iv]	$9.4^{+1.0}_{-0.9}$	1.7[c]	$5.3^{+0.5}_{-0.3}$	57.4/48
3C 105	0.089	12.0	[iv]	43^{+7}_{-6}	1.7[c]	220^{+90}_{-50}	13.6/12
3C 133	0.2775	25.0	[ii]	$0.8^{+0.4}_{-0.3}$	2.0 ± 0.3	190^{+80}_{-50}	39.4/26
3C 135	0.1253	8.7	[vi]	34^{+32}_{-19}	1.7[c]	14^{+23}_{-8}	15.8/13 C
3C 136.1[d]	0.064	32.0	[i]	–	1.7[c]	<0.06	–
3C 171	0.2384	5.7	[ii]	7 ± 1	1.5 ± 0.3	130^{+80}_{-50}	33.8/26
3C 180	0.22	14.0	[iii]	70^{+160}_{-50}	1.7[c]	90^{+1800}_{-70}	7.1/7 C
3C 184.1	0.1182	3.2	[iii]	8 ± 1	1.7[c]	110 ± 10	19.8/24
3C 192	0.0598	3.9	[iii]	34^{+8}_{-7}	1.7 ± 0.5	2^{+4}_{-1}	14.3/18
3C 223	0.1368	1.0	[iii]	13^{+13}_{-7}	1.7[c]	20^{+16}_{-8}	10/10 C
3C 223.1	0.107	1.3	[ii]	28 ± 6	1.7[c]	90^{+30}_{-20}	9.3/12 C
3C 234	0.1848	1.8	[vi]	17^{+9}_{-6}	1.7[c]	150^{+70}_{-50}	6.6/8
3C 277.3	0.0857	0.9	[xiii]	27^{+6}_{-5}	1.7[c]	9^{+2}_{-1}	23.1/21
3C 284	0.2394	0.9	[i]	<0.91	2.3 ± 1.0	$1.1^{+0.4}_{-0.5}$	1.4/5 C
3C 285	0.0794	1.3	[vi]	38^{+8}_{-6}	1.7[c]	35^{+10}_{-7}	7.7/11
3C 300	0.27	2.5	[i]	<0.19	1.4 ± 0.3	13 ± 2	12.7/10 C
3C 303.1	0.267	3.0	[ii]	18^{+132}_{-16}	1.7[c]	15^{+400}_{-11}	0.1/2 C
3C 305	0.0416	1.3	[viii]	<0.72	1.7[c]	0.04 ± 0.01	36.3/24 C
3C 321	0.096	3.8	[ix]	26^{+20}_{-13}	1.7[c]	4^{+4}_{-2}	61.2/40 C
3C 327	0.1041	5.9	[x]	30^{+63}_{-18}	1.7[c]	8^{+31}_{-4}	46.6/25
3C 379.1	0.256	5.4	[vi]	60^{+70}_{-30}	1.7[c]	110^{+400}_{-70}	7.3/8 C
3C 381	0.1605	9.9	[iii]	30^{+7}_{-6}	1.7[c]	240^{+70}_{-50}	18.9/21 C
3C 403	0.059	12.1	[xi]	46 ± 3	1.7[c]	78^{+10}_{-9}	51.5/57
3C 436	0.2145	6.7	[iii]	48^{+22}_{-15}	1.7[c]	100^{+80}_{-40}	14.4/15 C
3C 452	0.0811	9.8	[v]	53^{+8}_{-7}	1.7[c]	100 ± 20	77.9/78
3C 456	0.233	3.7	[ii]	7 ± 1	1.7[c]	160 ± 20	63.6/59 C
3C 458	0.289	5.9	[ii]	35^{+20}_{-16}	1.7[c]	150^{+140}_{-70}	16.8/14 C
3C 459	0.2199	5.2	[xii]	4^{+3}_{-2}	1.7[c]	12^{+3}_{-2}	31.2/25

[a]All the adopted models are absorbed by the Galactic column density: [i] po; [ii] zpha*po; [iii] zphabs*po + po; [iv] zphabs* (po + zgauss); [v] zphabs* (po+zgauss)+ po + pexrav); [vi] zphabs* (po+zgauss)+po; [vii] mekal; [viii] mekal + po; [ix] zphabs* (po+zgauss)+po + 2zgauss; [x] zphabs* (po+zgauss)+po + mekal; [xi] zphabs* (po +zgauss)+po+2zgauss + mekal; [xii] zphabs* (po)+po + mekal; [xiii] zphabs* (po+zgauss) + zphabs*po. [b]Statistics refers to the entire energy band assuming the model listed in column (4). 'C' indicates that the C-statistics was adopted. [c]Fixed photon index. [d]Luminosities estimated with PIMMS assuming a simple power-law model with $\Gamma = 1.7$.

Table 3. Spectral parameters of the soft X-ray component.

Name	Γ_S	kT (keV)	$L_{0.5-2}$ (10^{42} erg s^{-1})
	FR II-LERGs		
3C 88	$1.6 = \Gamma_H$	–	$0.03^{0.007}_{0.005}$
3C 173.1	$1.7 = \Gamma_H$	–	$0.3^{+0.3}_{-0.2}$
3C 196.1	–	$3.2^{+1.3}_{-0.8}$	9 ± 1
3C 288	–	$3.7^{+2.9}_{-1.2}$	$3.6^{+0.6}_{-0.5}$
3C 310	–	1.0 ± 0.2	$0.04^{+0.01}_{-0.009}$
3C 353	$1.7 = \Gamma_H$	–	0.04 ± 0.01
3C 357	$2 = \Gamma_H$	–	$0.9^{+0.7}_{-0.3}$
3C 388	–	$2.1^{+0.3}_{-0.2}$	$1.5^{+0.2}_{-0.1}$
3C 460	$1.7 = \Gamma_H$	–	0.7 ± 0.3
	FR II-HERGs/BLRGs		
3C 33	$1.7 = \Gamma_H$	–	$1.0^{+0.3}_{-0.2}$
3C 61.1	1.2 ± 1.0	–	0.7 ± 0.4
3C 79	$1.7 = \Gamma_H$	–	$1.8^{+1.0}_{-0.7}$
3C 135	2.2 ± 1.0	–	0.5 ± 0.2
3C 180	$1.7 = \Gamma_H$	–	$0.9^{+0.6}_{-0.4}$
3C 184.1	$1.7 = \Gamma_H$	–	0.7 ± 0.3
3C 192	$1.7 = \Gamma_H$	–	0.04 ± 0.01
3C 223	$1.7 = \Gamma_H$	–	1.4 ± 0.4
3C 234	2.3 ± 0.5	–	7 ± 1
3C 277.3	$1.7 = \Gamma_H$	–	$0.31^{+0.1}_{-0.08}$
	$N_{H,2} = 1.1^{+0.5}_{-0.4}$[a]		
3C 285	$1.7 = \Gamma_H$	–	0.14 ± 0.1
3C 305	–	0.8 ± 0.2	$0.013^{+0.006}_{-0.005}$
3C 321	2.8 ± 0.2	–	$0.8^{+0.07}_{-0.06}$
3C 327	$1.7 = \Gamma_H$	$0.20^{+0.04}_{-0.02}$	1.9 ± 0.1
3C 379.1	$1.7 = \Gamma_H$	–	$1.2^{+0.9}_{-0.7}$
3C 381	$1.7 = \Gamma_H$	–	$2. \pm 0.5$
3C 403	$1.7 = \Gamma_H$	0.20 ± 0.03	0.4 ± 0.04
3C 436	$1.7 = \Gamma_H$	–	0.4 ± 0.2
3C 452	$1.7 = \Gamma_H$	–	0.1 ± 0.04
3C 459	$1.7 = \Gamma_H$	$0.7^{+0.2}_{-0.1}$	$3.9^{+0.7}_{-0.6}$

[a]A secondary absorption component is also required for this source (see Worrall, Birkinshaw & Young 2016).

Table 4. Reprocessed features.

Name	Fe Kα line[a]	Reflection (R)
	FR II-LERGs	
3C 88	Unconstrained	–
3C 132	EW < 949	–
3C 165	EW < 776	–
3C 166	EW < 388	–
3C 173.1	EW ≥ 886	–
3C 213.1	Unconstrained	–
3C 236	EW < 572	–
3C 326	Unconstrained	–
3C 349	EW < 339	–
3C 353	EW $= 100 \pm 78$	–
3C 357	EW < 610	–
3C 401	Unconstrained	–
3C 460	EW < 359	–
	FR II-HERGs/BLRGs	
3C 20	EW < 281	–
3C 33	EW $= 139 \pm 89$	$R = 1.5^{+0.4}_{-0.6}$
3C 61.1	EW < 359	–
3C 79	EW < 157	–
3C 98	EW $= 277 \pm 135$	–
3C 105	EW $= 178 \pm 132$	–
3C 133	EW < 453	–
3C 135	EW$= 916^{+1474}_{-719}$	–
3C 171	EW < 117	–
3C 180	EW < 744	–
3C 184.1	EW < 278	–
3C 192	EW < 260	–
3C 223	EW < 836	–
3C 223.1	EW < 374	–
3C 234	EW $= 900 \pm 400$	–
3C 277.3	EW $= 200 \pm 100$	–
3C 284	Unconstrained	–
3C 285	EW $= 367^{+144}_{-47}$	–
3C 300	Unconstrained	–
3C 303.1	Unconstrained	–
3C 305	Unconstrained	–
3C 321	EW $= 988^{+751}_{-474}$	–
3C 327	EW $= 2000^{+3000}_{-742}$	–
3C 379.1	EW $= 557^{+1900}_{-464}$	–
3C 381	EW < 2304	–
3C 403	EW $= 153^{+60}_{-15}$	–
3C 436	EW < 591	–
3C 452	EW $= 172^{+65}_{-65}$	$R = 2^{+0.4}_{-0.5}$
3C 456	EW < 156	–
3C 458	EW < 238	–
3C 459	EW < 649	–

[a]Observed iron line equivalent width in eV.

deviation is 0.3 (see Table 2). Intrinsic cold gas obscuration was required in about 50 per cent of the sources. They are generally moderately absorbed, with a N_{HX} of the order of a few 10^{22} cm^{-2}. Only in two radio galaxies, i.e. 3C 173.1 and 3C 460, the column density reaches values of few 10^{23} cm^{-2}. An iron Kα line was detected in 3C 353 (see Table 4) with an intensity, within the large uncertainties, compatible with being produced by the same matter obscuring the nuclear region (Ghisellini, Haardt & Matt 1994). For the other objects with intrinsic absorption, the feature could not be revealed because of the low statistics and the abrupt drop of the *Chandra* effective area above 6–7 keV.

When present, the soft X-ray excess is well described by a power law, which is probably scattered nuclear emission. Indeed, the normalization values of the scattered component at 1 keV are always a few per cent of the absorbed one: the mean value is 6 per cent, in agreement with those measured for type 2 Seyferts (e.g. Bianchi & Guainazzi 2007).

The cluster emission, when present in the X-ray images, is generally dominant. In four cases (3C 196.1, 3C 288, 3C 310, and 3C 388), the AGN is overwhelmed by the thermal gas and any nuclear study is precluded. Therefore, for these sources, the estimated 2–10 keV luminosity should be considered as an upper limit of the nuclear AGN emission. Only in 3C 88, the AGN spectrum was disentangled from the thermal emission and it is analogous to that of the other absorbed radio galaxies. Instead, in 3C 401, the AGN emission dominates over the cluster one and the nuclear spectrum is well reproduced by a single power law. The intrinsic absorption is negligible, and, indeed, only an upper limit is provided (see Table 2).

The spectra of the control sample (FR II-HERGs/BLRGs) are generally more complex than FR II-LERGs (see Table 2). About 90 per cent of them show strong obscuration, with typical values one order of magnitude higher than FR II-LERGs ($N_H \sim 10^{23}$ cm^{-2}). The photon index could be well constrained in only 15 per cent (5

out of 32) of sources ($<\Gamma>$ =1.8 and $\sigma_{\rm rms}$ = 0.5). Intense iron lines with equivalent width (EW) spanning from 140 eV to more than 1 keV are detected in 11 sources, and, in at least two cases, a Compton reflection model was also required (Table 4). These reprocessed features, signature of a complex and inhomogeneous circumnuclear absorber, are commonly observed in Seyfert-like spectra (Risaliti 2002).

The soft X-ray excess of >50 per cent of FR II-HERGs/BLRGs is generally well reproduced by a second power law, which can be interpreted as the scattered component of the primary one. The mean unabsorbed normalization at 1 keV is 8 per cent of the absorbed one. In addition to the second power law, a MEKAL model is required in a few objects: in some cases, this component is directly related to collisional gas emission (cluster or shocked gas), and in the other ones, it could mimic photoionized features (Balmaverde et al. 2012). Indeed, in two RGs, i.e. 3C 403 and 3C 321, single soft X-ray emission lines associated with Ne IX, O VII, and Mg XI were revealed in the spectrum.

In summary, the control sample show more complex and feature-rich spectra than the key sample. FR II-HERGs/BLRGs are characterized by mean values of intrinsic absorption and X-ray luminosity one order of magnitude larger than FR II-LERGs, implying a substantially higher activity of the central engine and a more variegated circumnuclear environment.

4 DISCUSSION

The aim of the present study is to explore the jet–accretion connection and the role of the environment in shaping the radio morphology in sources of different FR types. Our X-ray results can be summarized as follows:

(i) Nearly 30 per cent of FR II-LERGs are in a dense/extended gaseous environment, as attested by the *Chandra* images. Thermal gas is also detected in several images of the FR II-HERGs/BLRGs control sample. The extension of the emission seems to suggest a galactic rather than an intergalactic origin;

(ii) FR II-LERGs' spectra are generally well modelled by a power law absorbed by a moderate intrinsic column density ($N_{\rm H} \sim 10^{22}$ cm^{-2}). Conversely, FR II-HERGs/BLRGs have spectra rich in features and engines obscured by high column densities ($N_{\rm H} \geq 10^{23}$ cm^{-2});

(iii) FR II-LERGs are intrinsically less luminous than FR II-HERGs/BLRGs by a factor of 10 in the 2–10 keV band.

4.1 Are FR II-LERGs obscured FR II-HERGs/BLRGs?

The first scenario that we explore supposes that FR II-LERGs could be obscured FR II-HERGs/BLRGs.

Our analysis does not support this hypothesis. The gas column densities, estimated from the X-ray spectra, carry out information on the environment down to sub-parsec scales. Looking at Table 2, the difference between the FR II classes in terms of $N_{\rm H}$ is evident: FR II-HERGs/BLRGs are more obscured than FR II-LERGs. A two-sample test univariate programme, TWOST (Feigelson & Nelson 1985; Isobe, Feigelson & Nelson 1986), which takes into account upper limits, confirms that the two samples are different, with $P_{\rm TWOST} = 7 \times 10^{-4}$. We assume $P_{\rm TWOST} = 0.05$ as the probability threshold to rule out the hypothesis that two samples are drawn from the same population.

To take a step forward, 3CR/FR I radio galaxies with X-ray information available from literature (Balmaverde, Capetti & Grandi 2006) were also compared to the FR II samples. The peak of the $N_{\rm H}$ distribution in FR Is is clearly shifted to lower values, as shown in Fig. 3. There is a partial overlap with FR II-LERGs. However, a TWOST test applied to FR II-LERGs and FR Is provides a probability of $P_{\rm TWOST} = 2 \times 10^{-2}$, showing that these two samples are intrinsically different. Instead, the same test confirms that FR II-HERGs/BLRGs and FR Is are drawn from different populations ($P_{\rm TWOST} < 10^{-4}$). It is interesting to note that larger amounts of cold gas column densities are associated to RGs with efficient accretion discs.

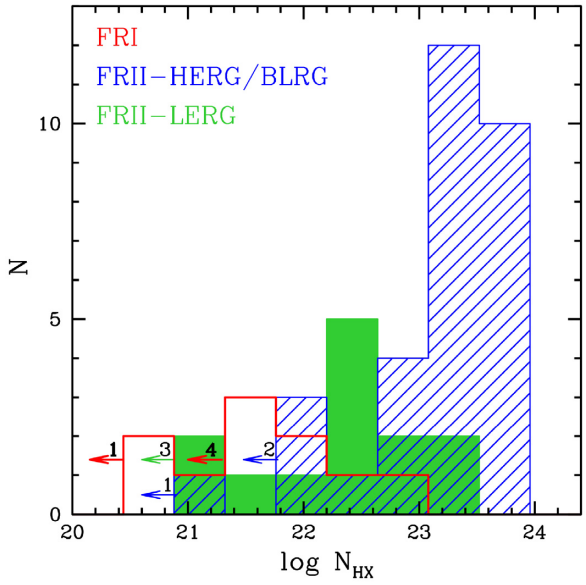

Figure 3. Distribution of the intrinsic gas column density $N_{\rm HX}$ in units of cm^{-2}, as measured in the X-ray band. The FR II-LERGs population (green) is, on average, less obscured than FR II-HERGs/BLRGs (blue), but more than FR Is (red). Arrows indicate upper limits with the number of sources per bin specified. FR I data are taken from Balmaverde et al. (2006).

We conclude that there is an indication that the quantity of obscuring matter (in the form of cold gas) is decreasing from FR II-HERGs/BLRGs to FR Is, with FR II-LERGs lying in between.

Another source of obscuration is the dust spread in the galaxy, which could affect our optical measurements. Note that the optical classification of RGs provided by Buttiglione et al. (2009) is based on lines produced in the NLR.

The dust content can be estimated using the Balmer decrement. Adopting an extinction curve $\kappa(\lambda)$, the intrinsic colour excess can be expressed as

$$E(B-V)_i = \frac{2.5}{[\kappa({\rm H}\beta) - \kappa({\rm H}\alpha)]} \times \log\left[\frac{({\rm H}\alpha/{\rm H}\beta)_{\rm o}}{3.1}\right].$$

Details on the derivation of the above formula can be found in the appendix of Momcheva et al. (2013). The theoretical (Hα/Hβ) ratio is 2.86, as expected if the temperature and the electron density of the NLR are $T = 10^4$ K and $N_{\rm e} = 10^3$ cm^{-3}, respectively (Osterbrock 1989). Actually, a value of 3.1 is considered the best prescription for AGN (Gaskell 1982, 1984; Wysota & Gaskell 1988; Tsvetanov & Iankulova 1989; Heard & Gaskell 2016). Several functional forms for the attenuation curve are present in literature. The most used are the Milky Way extinction curve (Cardelli, Clayton & Mathis 1989), the Large and Small Magellanic Cloud extinction curves from Gordon et al. (2003), and a general extragalactic extinction curve from Calzetti (1997). The reddening study was performed

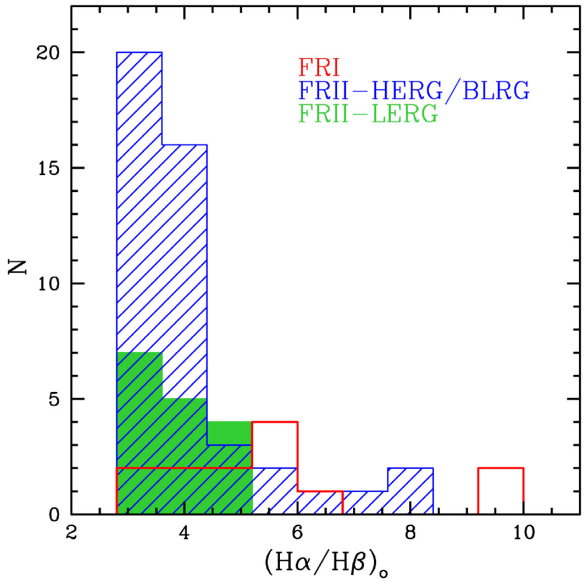

Figure 4. Distribution of the observed Balmer decrement $(H\alpha/H\beta)_o$ used to estimate the dust extinction for the three classes of RGs considered in this work, i.e. FR II-LERGs, FR II-HERGs/BLRGs, and FR Is. Hα and Hβ flux measurements are taken from Buttiglione et al. (2009). We assume the theoretical $(H\alpha/H\beta)_o = 3.1$ as a reliable value for AGN (see Section 4.1). When $(H\alpha/H\beta)_o < 3.1$, the source is considered unabsorbed.

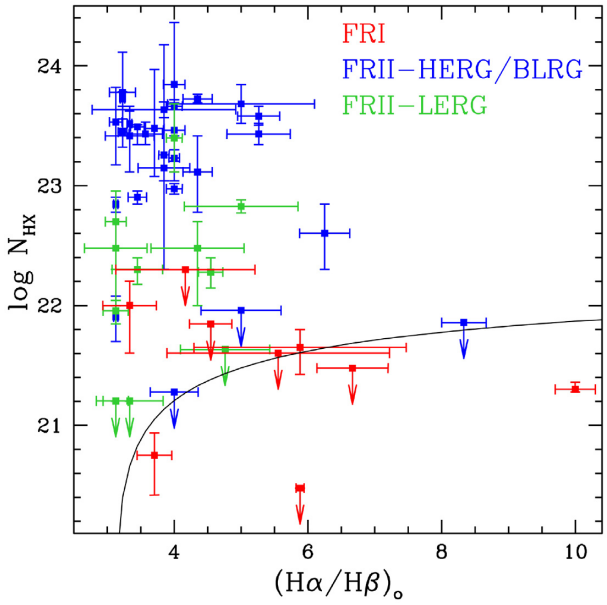

Figure 5. Column density (N_{HX}), as obtained by the X-ray analysis, plotted versus the intrinsic reddening, as measured by the optical Balmer decrement $(H\alpha/H\beta)_o$. N_{HX} decreases from FR II-HERGs/BLRGs to FR I. FR II-LERGs occupy the middle region of the plot. FR Is show the highest excess of colour and the lowest gas content. The black curve represents the expected N_H value assuming a dust-to-gas ratio $N_H/E(B-V) = 5.8 \times 10^{21}$ atoms cm^{-2} mag^{-1}.

considering all the different extinction curves. As the results are similar, hereafter, the discussion is based on the Milky Way extinction curve.

Buttiglione et al. (2010) provided the narrow Hα and Hβ fluxes for the majority of 3C RGs up to $z = 0.3$. We could then investigate the amount of dust in FR Is, FR II-LERGs and FR II-HERGs/BLRGs by simply comparing the $(H\alpha/H\beta)_o$ ratio (assuming the same extinction curves for all the galaxies). In Fig. 4, a histogram of the Balmer decrement for all the sources with detected lines (74 out of 79) is presented. When the flux ratio was less than the theoretical value, the source was considered unabsorbed (i.e. $(H\alpha/H\beta)_o = 3.1$). It is immediate to note that the FR Is' distribution peaks to higher values of $(H\alpha/H\beta)_o$. Indeed, a Kolmogorov–Smirnov (KS) test confirms that FR Is are richer in dust than both FR II-LERGs ($P_{KS} = 0.01$) and FR II-HERGs/BLRGs ($P_{KS} = 0.008$). The current optical data do not allow us to exclude that the two FR II classes are drawn from the same population ($P_{KS} = 0.32$).

Therefore, the difference between FR II-LERGs and FR II-HERGs/BLRGs is intrinsic and not an artefact due to different absorbing screens.

In Fig. 5, the column density (N_{HX}) measured in the X-ray band is plotted versus $(H\alpha/H\beta)_o$. This plot traces the obscuring matter at different scales: N_{HX} maps the gas down to sub-parsec scales, while the optical lines $(H\alpha/H\beta)_o$ (i.e. $E[B-V]$) carry out information from the NLR.

Different classes appear to populate distinct regions of the plot: FR II-HERGs/BLRGs, having higher N_{HX} values, mainly cluster in the upper part of the plot, FR II-LERGs occupy a similar region but are shifted to lower N_{HX}, and FR Is lie at the bottom of N_{HX} but extend to $(H\alpha/H\beta)_o$ up to 10. Moreover, all FR Is are at the edge or below the N_H line that traces the expected amount of gas according to a standard Galactic gas-to-dust ratio $N_H = 5.8 \times 10^{21}$ $E(B-V)$ atoms cm^{-2} mag^{-1} (Bohlin, Savage & Drake 1978). Conversely, all the FR IIs are above the N_H line, suggesting a large amount of gas (although with different column densities) near the BH and paucity of dust in the NLR and/or along the galaxy.

The dichotomy between FR II-LERGs and FR II-HERGs/BLRGs is reinforced by the X-ray analysis. The unabsorbed X-ray luminosity divided by the Eddington luminosity ($L_{Edd} = 1.3 \times 10^{38}$ $M/M_\odot$ erg s^{-1}) is a direct proxy of the accretion rate ($L_{2-10\,keV}/L_{Edd}$; Merloni, Heinz & di Matteo 2003). The BH masses for the sources in our sample were calculated by exploiting the relation between the H-band host-galaxy magnitude (taken from Buttiglione et al. 2009) and M_{BH}, provided by Marconi & Hunt (2003) (with a dispersion of ~ 0.3 dex in the BH mass). As expected, no significant difference in masses is observed among FR Is and FR IIs. The M_{BH} range is narrow: $10^{8.5}-10^{9.5}$ $M_\odot$.

The upper panel of Fig. 6 shows the $L_{2-10\,keV}/L_{Edd}$ distribution for the three classes. The distributions of FR Is and FR II-HERGs/BLRGs are clearly separated ($P_{TWOST} < 10^{-4}$), while FR II-LERGs are in between. The displacement of FR II-LERGs' peak towards lower accretion rates is confirmed by a TWOST test, which associates a probability of 10^{-4} and 5.8×10^{-3} to the hypothesis that FR II-LERGs are drawn from the same parent population of FR II-HERGs/BLRGs and FR Is, respectively. Therefore, the nuclear activity is inherently different in FR Is, FR II-LERGs, and FR II-HERGs/BLRGs.

Note that for RGs with an ADAF-like engine, the estimated X-ray luminosity could provide an upper limit of the accretion luminosity, as there could be a significant contribution from the jet emission. If this were the case, the separation between FR II-LERGS and FR II-HERGs/BLRGs would be even more pronounced. Finally, we note that the same trend is observed when the ionizing radiation L_{ion} in terms of the Eddington luminosity is considered (lower panel of Fig. 6). This quantity, defined as $\log L_{ion} \sim \log L_{[O\,III]} + 2.83$ (Buttiglione et al. 2009), is directly related to the accretion efficiency, being responsible for the excitation of the NLR gas.

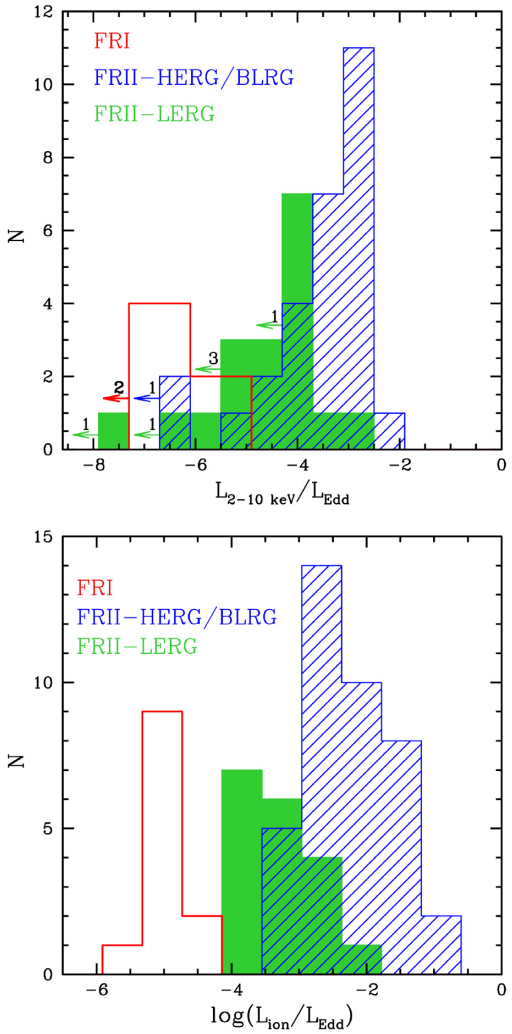

Figure 6. Upper panel: X-ray luminosity normalized for the Eddington luminosity. FR Is are in red, FR II-LERGs are in green, and FR II-HERGs/BLRGs are in blue. Leftwards arrows indicate upper limits, with a specified number per bin and population. Lower panel: estimated L_{ion}/L_{Edd} ratio. Both accretion rate estimates show the same trend: FR Is at the lowest values, classical FR IIs at the highest ones, and FR II-LERGs in between.

The agreement between upper and lower panels of Fig. 6 corroborates our previous conclusion based on the $(H\alpha/H\beta)_o$ study. As no dust correction was applied to L_{ion}, the different optical classification of FR IIs *cannot* be ascribed to optical NLR obscuration.

4.2 Were FR II-LERGs powerful FR II-HERGs/BLRGs in the past?

The comparison of the X-ray and $L_{[O\,III]}$ luminosities, accretion rates, and intrinsic nuclear absorption among the examined classes of sources has solidly established that FR II-LERGs have intermediate properties, lying between FR Is and FR II-HERGs/BLRGs. It is plausible that FR II-LERGs represent an evolutionary stage of FR II-HERGs/BLRGs. A link between the accretion properties and the power of the produced jets is certainly expected, based on both theoretical arguments (e.g. Blandford & Znajek 1977b; Sikora, Stawarz & Lasota 2007) and observational works (e.g. Allen et al. 2006; Ghisellini et al. 2014). Since the FR II-LERGs in this sample accrete at lower rates than classic FR II-HERGs/BLRGs, we would then expect their jets to be correspondingly less powerful. Contrary to these expectations, their extended radio luminosities, generally assumed as predictors of the total jet power (e.g. Cavagnolo et al. 2010a), are very similar (see Fig. 1). This conflict can be bypassed considering the large-scale radio structures of FR II-LERGs as the heritage of a past AGN activity at higher efficiency. If the nuclear activity has recently decreased due, for instance, to the depletion of the cold gas reservoir, it is reasonable to think that this information may not have reached the large-scale radio structures yet, which are formed at kilo-parsec distances from the central engine.

The evolutionary scenario is also supported by a recent analysis of a large sample of low-redshift and low-luminosity FR II objects (Capetti, Massaro & Baldi 2017), which showed that the roughly one-to-one correspondence between FR II morphologies and powerful nuclei is not verified for this large population in the local Universe ($z < 0.15$). On the contrary, most of the FR IIs in the catalogue compiled by Capetti et al. (2017) are classified as LERGs. This could suggest that the local FR IIs are 'starved', i.e. they now miss the fueling cold material that made them shine in the past.

4.3 Does the environment play a role?

Another possibility is that the nuclei of FR II-LERGs, while not as powerful as in classic FR II-HERGs/BLRGs, can still form FR II morphologies due to, for instance, favourable environmental conditions. Several studies in literature identify the environment as the fundamental ingredient for the origin of the FR I/FR II dichotomy. Gendre et al. (2013), studying the cluster richness (CR) for a large sample of RGs, suggest that the relation between radio morphology and accretion mode is quite complex and attributes to the environment an important role. They calculated the CR following the method of Wing & Blanton (2011), that is based on the count of galaxies within a disc of 1 Mpc of radius around each analysed target. Then, they concluded that FR II-HERGs/BLRGs and FR Is live in different ambients, being characterized by poor and rich environments, respectively. On the contrary, they found that the 29 FR II-LERGs of their sample can live both in clusters (≈40 per cent) and in scarcely populated regions (in terms of richness, ≈60 per cent).

Our X-ray data confirm that FR II-LERGs can actually be set in a dense and hot medium. Indeed, 6 out of 19 are found in clusters (see Fig. 2). Unfortunately, our X-ray analysis, exploiting data from public archives, suffers from an inhomogeneity of the exposure times, which prevents a comparative study on the environments among the different classes. Taking advantage of the richness study of Gendre et al. (2013), we could explore the relation between accretion, in terms of $L_{2-10\,keV}/L_{Edd}$, radio morphology and environment for 18 FR II-HERGs/BLRGs, 8 FR Is, and 9 FR II-LERGs. In Fig. 7 the X-ray luminosity scaled for the Eddington luminosity is plotted as a function of CR for the three classes. The vertical line is the limit between poor ($CR < 30$) and rich ($CR > 30$) environments proposed by Gendre et al. (2013). As expected, FR II-HERGs/BLRGs occupy the upper-left corner (i.e. they are in less dense environments and have more efficient engines), while FR Is are segregated in the lower-right region (i.e. they have high CR and low $L_{2-10\,keV}/L_{Edd}$ values). The intermediate accretion rates of FR II-LERGs put them in the middle part of the diagram, but, unlike the other classes, they fall into both sides of the threshold fixed at $CR = 30$. More impressive is the clear link in the whole sample

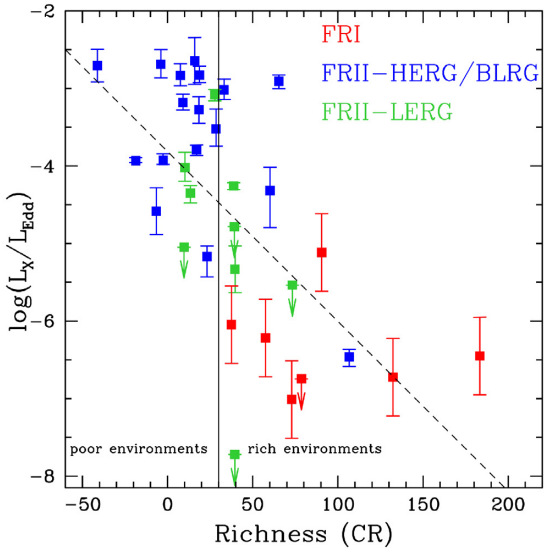

Figure 7. Environmental richness (CR) plotted versus the intrinsic Eddington-scaled X-ray luminosity. Colour coding is the same of previous figures. Downwards arrows indicate upper limits. The solid black line is the threshold between poor and rich environments (CR = 30), as indicated by Gendre et al. (2013). The dashed line represents the linear regression of data computed with ASURV parametric EM algorithm, including upper limits. The equation is $\log(L_X/L_{Edd}) = -(0.022 \pm 0.005) \times CR - (3.8 \pm 0.3)$.

between the richness of the environment and the accretion in terms of $L_{2-10\,keV}/L_{Edd}$. A Kendall$-\tau$ test in ASURV provides a very high probability that these quantities are correlated ($P_{Kendall-\tau} > 99.9$ per cent). With the appropriate caution required by the limited number of sources, this result suggests that the environment would have a strong impact on the accretion regime.

The problem with this interpretation is that the radio luminosity of the extended components, related to the jet kinetic power, is similar in FR IIs, at odds with what is observed in X-rays, where FR II-HERGs/BLRGs are brighter (more efficient accretors) than FR II-LERGs.

However, the relation $P_{jet} \propto L_{151\,MHz}^{6/7}$, proposed by Willott et al. (1999) and widely used in literature, is calibrated on FR II radio galaxies and suffers from large uncertainties represented by a factor $f^{3/2}$, which mainly depends on the ratio between the energy in protons and electrons in the lobes. Willott et al. (1999) deduced that f can span from 1 to 20, implying a P_{jet} uncertainty of about two orders of magnitude. Other authors revisited this relation measuring the jet power using the X-ray cavities produced by the interaction of FR I jets (Bîrzan et al. 2008; Cavagnolo et al. 2010b) or the hotspot size and an equipartition magnetic field in FR IIs (Godfrey & Shabala 2013). In particular, Cavagnolo et al. (2010b) concluded that a k-value larger than 100 is necessary to match with the relation proposed by Willott. Therefore, different classes of sources can require different values of f. We note that increasing f-values from FR Is to FR II-LERGs and FR II-HERGs/BLRGs could indeed maintain the proportionality between jet power and accretion luminosity.

Indeed, we note that the radio luminosity of a radio source can be amplified by radiative losses if the jet propagates through a dense environment. As claimed by Barthel & Arnaud (1996) on the basis of a Cygnus A study, this effect would amplify the radio luminosity and, in turn, weaken its reliability as an estimator of the AGN power.

5 CONCLUSIONS

The comparison of the optical/X-ray luminosities, accretion rates, and intrinsic nuclear absorption between the three examined classes of sources (FR Is, FR II-LERGs, FR II-HERGs/BLRGs) have solidly established that FR II-LERGs have intermediate properties. The measurement of moderate gas column densities in FR II-LERGs, combined with a modest dust reddening, enables us to directly reject the first discussed scenario (see Section 4.1), in which FR II-LERGs are a highly obscured version of classical powerful FR IIs.

Instead, the moderate N_H column densities and X-ray/[O III] luminosities are indicative of a weak nuclear activity with respect to the more obscured FR II-HERGs/BLRGs.

This leads at least to two different interpretations: (i) FR II-LERGs are 'starved' classical FR II-HERGs/BLRGs, or (ii) they are a separate class of RGs with their own properties.

In both cases, assuming a P_{jet}–L_{radio} relation, FR II jets appear to carry out similar amount of energy independently on their optical classification (and different X-ray luminosities). This is difficult to explain within the paradigm that assumes powerful jets produced by efficient accretors.

In the former case, this apparent disagreement could be explained if FR II-LERGs are switching from an efficient to an inefficient regime and this information may not have reached the lobe scales yet. In the latter case, the different trend of radio (jet power) and X-ray luminosities (accretion power) can be reconciled if the usually adopted P_{jet}–L_{radio} relation does not properly take into account the jet interaction with the surrounding medium.

ACKNOWLEDGEMENTS

The authors wish to thank the anonymous referee for constructive comments which helped to improve the paper.

DM and ET acknowledge financial contribution from the agreement ASI-INAF no. 2017-14-H.O.

REFERENCES

Abramowicz M. A., Chen X., Kato S., Lasota J.-P., Regev O., 1995, ApJ, 438, L37
Allen S. W., Dunn R. J. H., Fabian A. C., Taylor G. B., Reynolds C. S., 2006, MNRAS, 372, 21
Arnaud K. A., 1996, in Jacoby G. H., Barnes J., eds, ASP Conference Ser. Vol. 101, Astronomical Data Analysis Software and Systems V. Astron. Soc. Pac., San Francisco. p. 17
Avni Y., 1976, ApJ, 210, 642
Balmaverde B., Capetti A., Grandi P., 2006, A&A, 451, 35
Balmaverde B. et al., 2012, A&A, 545, A143
Barthel P. D., Arnaud K. A., 1996, MNRAS, 283, L45
Bennett A. S., 1962, Mem. RAS, 68, 163
Bianchi S., Guainazzi M., 2007, in di Salvo T., Israel G. L., Piersant L., Burderi L., Matt G., Tornambe A., Menna M. T., eds, AIP Conf. Proc. Vol. 924, The Multicolored Landscape of Compact Objects and Their Explosive Origins. Am. Inst. Phys., New York, p. 822
Bîrzan L., McNamara B. R., Nulsen P. E. J., Carilli C. L., Wise M. W., 2008, ApJ, 686, 859
Blandford R. D., Payne D. G., 1982, MNRAS, 199, 883
Blandford R. D., Znajek R. L., 1977a, MNRAS, 179, 433
Blandford R. D., Znajek R. L., 1977b, MNRAS, 179, 433
Bohlin R. C., Savage B. D., Drake J. F., 1978, ApJ, 224, 132
Burgess A. M., Hunstead R. W., 2006a, AJ, 131, 100
Burgess A. M., Hunstead R. W., 2006b, AJ, 131, 114

Buttiglione S., Capetti A., Celotti A., Axon D. J., Chiaberge M., Macchetto F. D., Sparks W. B., 2009, A&A, 495, 1033
Buttiglione S., Capetti A., Celotti A., Axon D. J., Chiaberge M., Macchetto F. D., Sparks W. B., 2010, A&A, 509, A6
Buttiglione S., Capetti A., Celotti A., Axon D. J., Chiaberge M., Macchetto F. D., Sparks W. B., 2011, A&A, 525, A28
Calzetti D., 1997, AJ, 113, 162
Capetti A., Massaro F., Baldi R. D., 2017, A&A, 601, A81
Cardelli J. A., Clayton G. C., Mathis J. S., 1989, ApJ, 345, 245
Cash W., 1979, ApJ, 228, 939
Cavagnolo K. W., McNamara B. R., Nulsen P. E. J., Carilli C. L., Jones C., Bîrzan L., 2010a, ApJ, 720, 1066
Cavagnolo K. W., McNamara B. R., Nulsen P. E. J., Carilli C. L., Jones C., Bîrzan L., 2010b, ApJ, 720, 1066
Celotti A., Padovani P., Ghisellini G., 1997, MNRAS, 286, 415
Evans D. A., Worrall D. M., Hardcastle M. J., Kraft R. P., Birkinshaw M., 2006, ApJ, 642, 96
Fabbiano G., Kim D. W., Trinchieri G., 1992, ApJS, 80, 531
Fanaroff B. L., Riley J. M., 1974, MNRAS, 167, 31P
Feigelson E. D., Nelson P. I., 1985, ApJ, 293, 192
Ferrarese L., Merritt D., 2000, ApJ, 539, L9
Gaskell C. M., 1982, PASP, 94, 891
Gaskell C. M., 1984, Astrophys. Lett., 24, 43
Gebhardt K. et al., 2000, ApJ, 539, L13
Gendre M. A., Best P. N., Wall J. V., Ker L. M., 2013, MNRAS, 430, 3086
Ghisellini G., 2010, in Bertin G., de Luca F., Lodato G., Pozzoli R., Romé M., eds, AIP Conf. Proc. Vol. 1242, Plasmas in the Laboratory and in the Universe: Interactions, Patterns, and Turbulence. Am. Inst. Phys., New York. p. 43
Ghisellini G., Haardt F., Matt G., 1994, MNRAS, 267, 743
Ghisellini G., Tavecchio F., Maraschi L., Celotti A., Sbarrato T., 2014, Nature, 515, 376
Godfrey L. E. H., Shabala S. S., 2013, ApJ, 767, 12
Gopal-Krishna, Wiita P. J., 2000, A&A, 363, 507
Gordon K. D., Clayton G. C., Misselt K. A., Land olt A. U., Wolff M. J., 2003, ApJ, 594, 279
Grandi P., Malaguti G., Fiocchi M., 2006, ApJ, 642, 113
Greene J. E., Ho L. C., 2005, ApJ, 627, 721
Greene J. E., Ho L. C., 2006, ApJ, 641, L21
Heard C. Z. P., Gaskell C. M., 2016, MNRAS, 461, 4227
Heckman T. M., Best P. N., 2014, ARA&A, 52, 589
Isobe T., Feigelson E. D., Nelson P. I., 1986, ApJ, 306, 490
Kalberla P. M. W., Burton W. B., Hartmann D., Arnal E. M., Bajaja E., Morras R., Pöppel W. G. L., 2005, A&A, 440, 775
Komatsu E. et al., 2009, ApJS, 180, 330
Kormendy J., 1993, in Dejonghe H., Habing H. J., eds, Proc. IAU Symp. 153, Galactic Bulges. Kluwer, Dordrecht. p. 209
Kormendy J., 2004, in Ho L. C., ed., Carnegie Obs. Astrophys. Ser. Vol. 1, Coevolution of Black Holes and Galaxies. Cambridge Univ. Press, Cambridge. p. 1
Kraft R. P., Azcona J., Forman W. R., Hardcastle M. J., Jones C., Murray S. S., 2006, ApJ, 639, 753
Kraft R. P. et al., 2012, ApJ, 749, 19
Laing R. A., Riley J. M., Longair M. S., 1983, MNRAS, 204, 151
Laing R. A., Jenkins C. R., Wall J. V., Unger S. W., 1994, in Bicknell G. V., Dopita M. A., Quinn P. J., eds, ASP Conf. Ser. Vol. 54, The Physics of Active Galaxies. Astron. Soc. Pac., San Francisco. p. 201
Lal D. V. et al., 2010, ApJ, 722, 1735
Lightman A. P., White T. R., 1988, ApJ, 335, 57
Liu W. et al., 2019, MNRAS, 484, 3376
Magorrian J. et al., 1998, AJ, 115, 2285
Maraschi L., Tavecchio F., 2003, ApJ, 593, 667
Marconi A., Hunt L. K., 2003, ApJ, 589, L21
Massaro F. et al., 2010, ApJ, 714, 589
Massaro F. et al., 2012, ApJS, 203, 31
McConnell N. J., Ma C.-P., Gebhardt K., Wright S. A., Murphy J. D., Lauer T. R., Graham J. R., Richstone D. O., 2011, Nature, 480, 215
Merloni A., Heinz S., di Matteo T., 2003, MNRAS, 345, 1057
Momcheva I. G., Lee J. C., Ly C., Salim S., Dale D. A., Ouchi M., Finn R., Ono Y., 2013, AJ, 145, 47
Morganti R., Killeen N. E. B., Tadhunter C. N., 1993, MNRAS, 263, 1023
Narayan R., Yi I., 1994, ApJ, 428, L13
Narayan R., Mahadevan R., Grindlay J. E., Popham R. G., Gammie C., 1998, ApJ, 492, 554
Osterbrock D. E., 1989, Astrophysics of Gaseous Nebulae and Active Galactic Nuclei. University Science Books, Mill Valley, CA
Padovani P., 2016, A&AR, 24, 13
Rawlings S., Saunders R., 1991, Nature, 349, 138
Reynolds C. S., Brenneman L. W., Stocke J. T., 2005, MNRAS, 357, 381
Ricci F. et al., 2018, ApJ, 867, 35
Risaliti G., 2002, A&A, 386, 379
Shakura N. I., Sunyaev R. A., 1973, A&A, 500, 33
Sikora M., Stawarz Ł., Lasota J.-P., 2007, ApJ, 658, 815
Spinrad H., Djorgovski S., Marr J., Aguilar L., 1985, PASP, 97, 932
Tadhunter C., 2016, A&AR, 24, 10
Tremaine S. et al., 2002, ApJ, 574, 740
Tsvetanov Z. I., Iankulova I. M., 1989, MNRAS, 237, 707
Wall J. V., Peacock J. A., 1985, MNRAS, 216, 173
Willott C. J., Rawlings S., Blundell K. M., Lacy M., 1999, MNRAS, 309, 1017
Wing J. D., Blanton E. L., 2011, AJ, 141, 88
Worrall D. M., Birkinshaw M., Young A. J., 2016, MNRAS, 458, 174
Wysota A., Gaskell C. M., 1988, in Miller H. R., Wiita P. J., eds, Proc. Conf. Georgia State University, Reddening of Narrow Line Regions. Springer-Verlag, Berlin. p. 79

This paper has been typeset from a TEX/LATEX file prepared by the author.